ACSNANO

www.acsnano.org

ARTICLE

9,10-Phenanthrenequinone: A Promising Kernel to Develop Multifunctional Antitumor Systems for Efficient Type I Photodynamic and Photothermal Synergistic Therapy

Jingjing Guo,[▽] Jun Dai,[▽] Xiaoluo Peng, Quan Wang, Shixuan Wang, Xiaoding Lou, Fan Xia, Zujin Zhao,* and Ben Zhong Tang

Cite This: https://doi.org/10.1021/acsnano.1c07730

ABSTRACT: Synergistic phototherapy provides a promising strategy to conquer the hypoxia and heterogeneity of tumors and realize a better therapeutic effect than monomodal photodynamic therapy (PDT) or photothermal therapy (PTT). The development of efficient multifunctional organic phototheranostic systems still remains a challenging task. Herein, 9,10-phenanthrenequinone (PQ) with strong electron-withdrawing ability is conjugated with the rotor-type electron-donating triphenylamine derivatives to create a series of tailor-made photosensitizers. The highly efficient Type I reactive oxygen species generation and outstanding photothermal conversion capacity are tactfully integrated into these PQ-cored photosensitizers. The underlying photophysical and photochemical mechanisms of the combined photothermal and Type I photodynamic effects are deciphered by experimental and theoretical methods and are closely associated with the active intramolecular bond stretching vibration, facilitated intersystem crossing, and specific redox cycling activity of the PQ core. Both *in vitro* and *in vivo* evaluations demonstrate that the nanoagents fabricated by these PQ-based photosensitizers are excellent candidates for Type I photodynamic and photothermal combined antitumor therapy. This study thus broadens the horizon for the development of high-performance PTT/Type I PDT nanoagents for synergistic phototheranostic treatments.

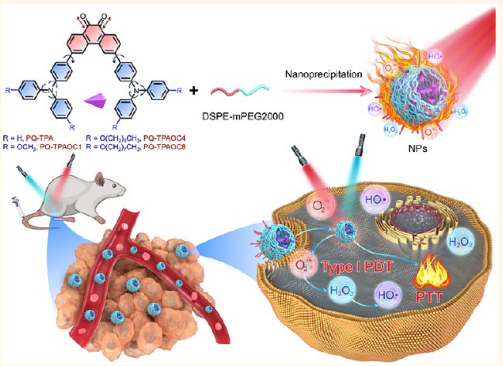

KEYWORDS: *9,10-phenanthrenequinone, Type I reactive oxygen species, photothermal conversion, intersystem crossing, redox cycling activity, bond stretching vibration, synergistic therapy*

INTRODUCTION

Phototheranostics, as a noninvasive precision medicine technology, provides great potential to realize real-time diagnosis and concurrent *in situ* treatment, and thus, it has recently attracted considerable attention in clinical malignant tumor elimination research.[1−3] Significant progress has been made in the development of phototheranostic systems nowadays, mainly including photothermal therapy (PTT) and photodynamic therapy (PDT).[4−6] Thereinto, PTT refers to the conversion of absorbed photonic energy into thermal energy, causing local high temperature to ultimately kill tumor cells with the advantages of high specificity, precise controllability, and minimal damage to normal tissues.[7−9] PDT, as another method of treating tumor disease, mainly utilizes photosensitizers to generate high levels of cytotoxic reactive oxygen species (ROS), which can lead to malignant tumor death by causing irreversible oxidative damage to biological macromolecules (DNA, proteins, lipids, etc.) and cell metabolic disorders.[10−12] Generally, a high oxygen (O_2) concentration level is the prerequisite to ensure a therapeutic effect of clinical PDT based on the Type II pathway.[13] However, the extremely hypoxia nature of tumor tissues is a common hallmark due to insufficient blood supply, and what is more, the O_2 consumption during PDT would further aggravate tumor hypoxia.[14,15] To overcome the Achilles' heel

Received: September 3, 2021
Accepted: November 24, 2021

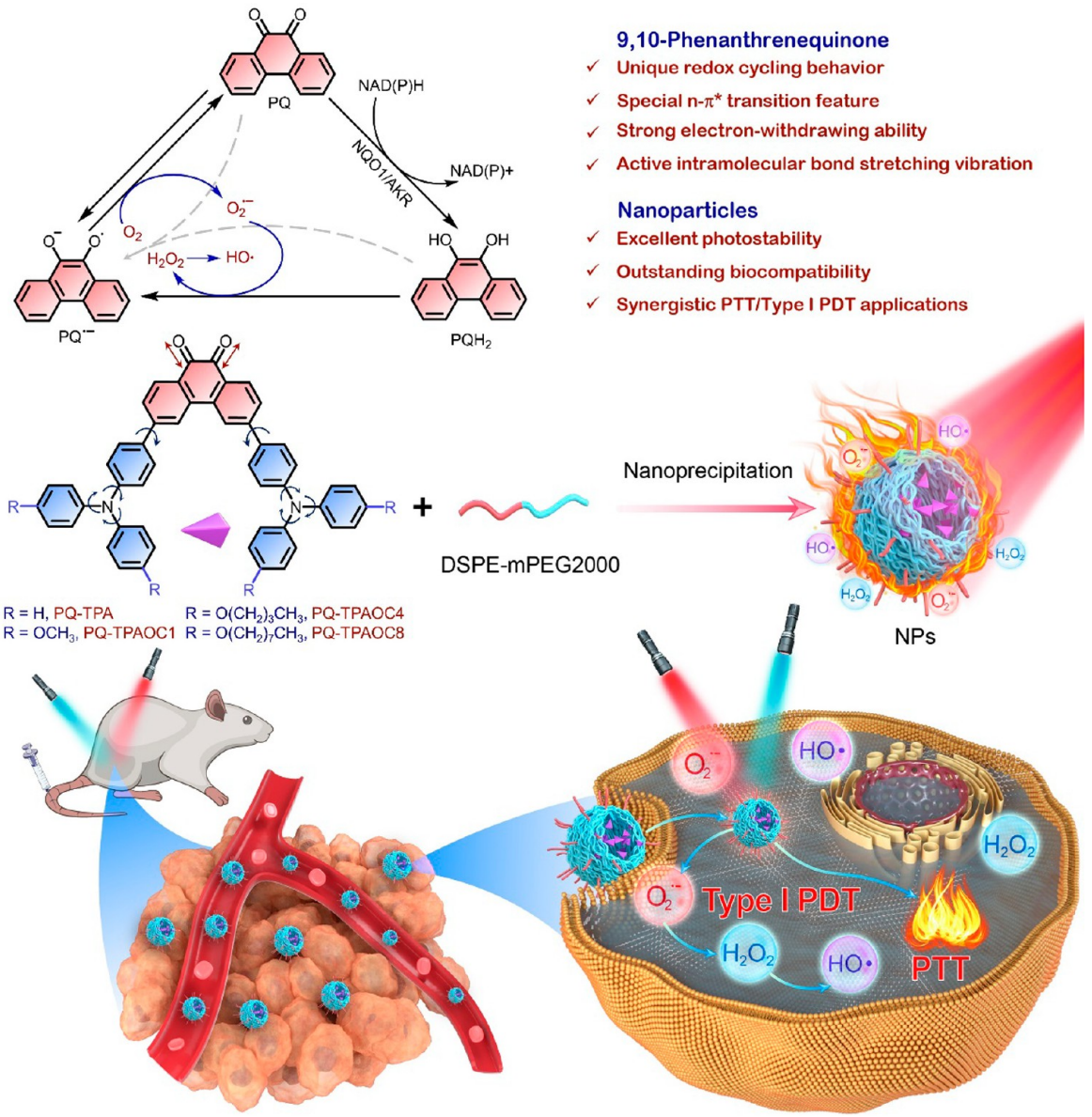

Figure 1. Redox cycling of PQ, schematic illustration of molecular structures, nanofabrication, and the synergistic PTT/Type I PDT tumor theranostics.

of traditional PDT, several O_2-replenishing strategies have been proposed, but often with complex therapy methods and severe side effects.[16,17] By contrast, the hypoxia-tolerant Type I PDT provides a straightforward way to improve tumor treatment efficacy, which can produce highly cytotoxic free radicals and thus perform well even under low O_2 conditions.[18−20] In addition, some studies confirmed that PTT could not only enhance vascular saturated O_2 concentration by increasing blood flow rate but also result in higher uptake of PDT agents by tumor cells, which are conducive to improving overall treatment efficacy.[21,22] But this desired therapeutic effect by the synergistic therapy can be hardly achieved by a monotherapy method. Therefore, the combination of Type I PDT and PTT is considered as a more feasible strategy to conquer the hypoxia and heterogeneity of tumors and realize a better antitumor therapy effect.

Phototherapy agents account for an essential component in phototheranostic applications. To date, most reported phototherapy agents applied in synergistic therapy are inorganic materials with various components, and only a few of them exhibit Type I PDT.[23−25] Their complicated composition, slow metabolism, and low reproducibility inevitably result in a limitation for practical clinical applications. In comparison with inorganic nanoagents, organic small molecules hold more advantages of simple composition, definite structure, outstanding biocompatibility, and adjustable functionality.[26−28] Aiming to achieve the purpose of highly efficient combination therapy, the ingenious construction of multifunctional organic small molecules with excellent Type I ROS generation and high photothermal conversion efficiency by balancing multiple competitive excited-state relaxation processes is of significant importance but will be a challenging task.

The Type I PDT mechanism is demonstrated to involve an electron transfer process between the photosensitizers at the triplet state and the substrate molecules to generate free radical ROS (Scheme S1), which means efficient intersystem crossing (ISC) and intramolecular charge transfer (ICT) of the photosensitizers upon photoexcitation play key roles.[29−31]

https://doi.org/10.1021/acsnano.1c07730
ACS Nano XXXX, XXX, XXX−XXX

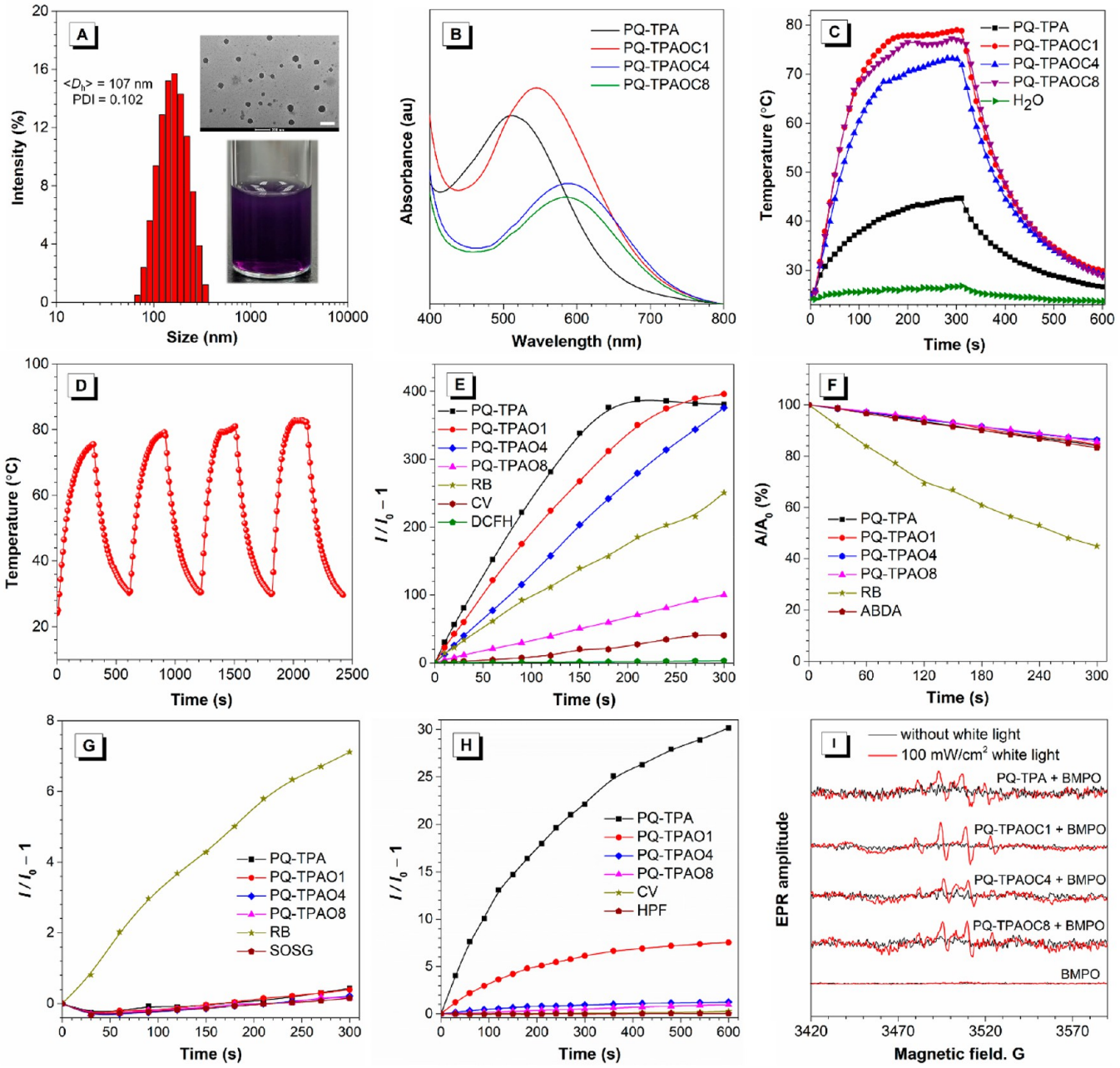

Figure 2. (A) Dynamic light scattering (DLS) profile of PQ-TPAOC1 NPs. Inset: the average hydrodynamic diameter (D_h) and PDI of PQ-TPAOC1 NPs measured by DLS; photograph of PQ-TPAOC1 NPs taken under room light and TEM image of PQ-TPAOC1 NPs (scale bar: 200 nm). (B) UV−vis absorption spectra of these NPs in water. (C) Photothermal curves of these NPs in aqueous solution (150 μM) and pure water upon 660 nm laser irradiation (800 mW cm^{-2}) for 300 s, and cooled for 300 s without irradiation. (D) Photothermal curves of PQ-TPAOC1 NPs subjected to four 660 nm laser irradiation on/off cycles at 800 mW cm^{-2}. Plots of (E) relative PL intensity ($I/I_0 - 1$) of DCFH (1 μM), (F) relative decomposition rates (A/A_0) of ABDA (30 μM), (G) relative PL intensity of SOSG (5 μM), and (H) HPF (5 μM) in the presence of 1 μM PQ-TPA NPs, PQ-TPAOC1 NPs, PQ-TPAOC4 NPs, PQ-TPAOC8 NPs, RB NPs, and/or CV NPs in PBS, upon white light irradiation with 50 mW cm^{-2} for different times. (I) ESR signals of BMPO (25 mM) in the presence 10 μM PQ-TPA, PQ-TPAOC1, PQ-TPAOC4, and PQ-TPAOC8 in PBS with 1 vol % DMSO, with/without white light irradiation (100 mW cm^{-2}) for 5 min. I_0 and I are the PL intensities of the indicator before and after irradiation, respectively. A_0 and A are the absorbances of ABDA before and after irradiation, respectively.

On the other hand, the active intramolecular motions mainly including rotations and vibrations are in favor of nonradiative energy dissipation, namely heat generation.[32] Thus, the introduction of sufficient molecular rotors and/or vibrators is very helpful for PTT. Especially, the high-frequency intramolecular bond stretching vibrations exhibit a more prominent advantage in boosting heat generation in the aggregated state, because they can occur in a confined space and can hardly be restricted by external environmental factors.[33,34]

Based on the above considerations, the molecular design strategy of creating organic molecules with electron donor−acceptor (D−A) interaction by choosing 9,10-phenanthrenequinone (PQ) that bears two carbonyl groups comes into being. The strong electron-withdrawing ability and special

https://doi.org/10.1021/acsnano.1c07730
ACS Nano XXXX, XXX, XXX−XXX

n−π^* transition feature of PQ can promote the ICT and ISC processes of the molecules.[35,36] And the active C═O double bond stretching vibration in PQ can also contribute significantly to nonradiative relaxation of the excited state. More importantly, PQ possesses active redox cycling activity, as shown in Figure 1. The semiquinone anion radical ($PQ^{\bullet-}$) can be easily formed by photoinduced self-electron transfer between the triplet PQ and adjacent substrates,[37] which undergoes electron transfer with O_2 to produce superoxide anion radical ($O_2^{\bullet-}$). The $O_2^{\bullet-}$ further reacts with superoxide dismutase (SOD) inside tumor cells to form hydrogen peroxide (H_2O_2), which is subsequently converted to highly toxic hydroxyl radical (HO•).[38,39] By two-electron reduction of PQ in the presence of NAD(P)H quinone oxidoreductase (NQO1) or aldo-keto reductase (AKR) isozymes, 9,10-phenanthrene hydroquinone (PQH_2) is attained, which can also interact with PQ through a disproportionation reaction to yield $PQ^{\bullet-}$. Additionally, PQH_2 can be oxidized back to $PQ^{\bullet-}$ with the production of H_2O_2, thus forming a redox cycle that renders superb generation of Type I ROS.[40,41]

Therefore, a series of PQ-cored molecules with a symmetric D−A−D molecular architecture are designed and synthesized (Figure 1). The rotor-type triphenylamine (TPA) derivatives are conjugated with the PQ vibrator to ensure active intramolecular motions even in the aggregated state for efficient heat generation under photon excitation. The n−π^* transition of carbonyl groups and strong ICT between electron-withdrawing PQ and electron-donating TPA derivatives are conducive to facilitating an ISC process. In addition, the introduction of methoxy or longer alkoxy chains into TPA can further regulate the strength of the ICT effect and the intermolecular spatial distance for simultaneously realizing high Type I ROS generation capacity and photothermal conversation efficiency in the aggregated state. To enhance the biocompatibility and dispersibility in aqueous solutions of these multifunctional organic molecules, water-soluble nanoparticles (NPs) are fabricated by encapsulating them within a polymeric matrix via a simple nanoprecipitation method. These NPs exhibit excellent performances of Type I ROS generation and photothermal conversation, and the underlying mechanisms are investigated in detail by combining the photophysical measurements and theoretical calculations. Finally, *in vitro* and *in vivo* experiments demonstrate that the synergistic PTT/Type I PDT treatment based on the NPs can achieve outstanding antitumor efficacy, validating the great potentials of these PQ-cored molecules in biomedical applications.

RESULTS AND DISCUSSION

Synthesis and Characterization. Four PQ-cored molecules, PQ-TPA, PQ-TPAOC1, PQ-TPAOC4, and PQ-TPAOC8, are facilely obtained through one-step Suzuki−Miyaura coupling reactions with satisfactory yields. Their chemical structures are confirmed by nuclear magnetic resonance spectroscopy and high-resolution mass spectrometry (Figures S1−S8). Single crystals of PQ-TPA are obtained from a dichloromethane (DCM)/ethanol mixture by slow solvent evaporation, and the X-ray crystallographic result further validates the molecular structure. The detailed synthetic procedures and corresponding characterization data are presented in the Supporting Information.

Electrochemical Behaviors. The redox properties of these PQ-cored molecules are investigated by cyclic voltammetry in *N*,*N*-dimethylformamide (DMF). As shown in Figure S9, PQ-TPA, PQ-TPAOC1, PQ-TPAOC4, and PQ-TPAOC8 undergo two successive one-electron reduction steps, generating two separated cathodic waves with the formation of the corresponding semiquinone anion radical and dianion. According to the first electron transfer process, the electrochemical parameters such as half-wave potentials ($E_{1/2}$), cathodic and anodic peak potentials (E_{pc}, E_{pa}), and cathodic and anodic peak current values (I_{pc}, I_{pa}) are obtained (Table S1). Taking PQ-TPAOC1 as an example, the values of the peak potentials (ΔE_p) and $E_{pc} - E_{1/2}$ are calculated to be 75 and −37 mV, respectively, which are approximate to the theoretical one-electron reversible reduction (57 and −28.5 mV).[42,43] Likewise, the ratio of the peak currents (I_{pa}/I_{pc}) is close to unity (0.95), indicating the production of relatively stable reduction intermediates.[42,44] Apparently, the quinone/semiquinone redox couple is reversible for these PQ-cored molecules. The reductively activated anion radicals have great potential to undergo redox cycling, which can promote the electron transfer process with O_2 to generate Type I ROS.[45,46]

Optical Properties. For the biological application, the water solubility of the agents is of high importance. To fulfill the application requirement in aqueous media, these PQ-cored molecules are fabricated into NPs using the amphiphilic polymer 1,2-distearoyl-*sn*-glycero-3-phosphoethanolamine-*N*-[methoxy-(polyethylene glycol)-2000] (DSPE-mPEG2000) as the encapsulation matrix by the nanoprecipitation method. The encapsulation efficiency of PQ-TPAOC1 NPs can be up to 94% with a well-dispersible spherical morphology, as displayed in the transmission electron microscopy (TEM) image. And the average hydrodynamic diameter of the NPs is about 107 nm, measured by dynamic light scattering (DLS) (Figure 2A), similar to the mean particle size of 81 nm observed from the TEM image (Figure S10), which is conducive to the accumulation of NPs in tumor tissues via the enhanced permeability and retention (EPR) effect.[47,48] The NPs of the other three molecules have similar hydrodynamic diameters in the range of 126−154 nm (Figure S11).

As illustrated in Figure 2B, these NPs in water show ICT broad absorption bands extending to 800 nm, which is helpful for biological applications *in vivo*. The introduction of the electron-rich oxygen atoms and alkyl chain improves the electron-donating ability of TPA, resulting in a stronger ICT effect. Thus, the maximum absorption peaks of PQ-TPAOC4 NPs and PQ-TPAOC8 NPs (~588 nm) exhibit a more obvious bathochromic shift (76 nm) than that of PQ-TPA NPs, which is consistent with the trend of the molecular absorption spectra in tetrahydrofuran (THF) solutions (Figure S12). The excellent light-harvesting abilities of these NPs are favorable in making the best use of excited-state energy for multimodal synergistic therapy. Moreover, the absorption spectra of these NPs in aqueous solutions remain almost unchanged upon continuous white light and/or laser irradiation for 5 min (Figure S13), suggesting high photostability. Especially for PQ-TPAOC1 NPs, the absorption spectrum and DLS analysis results show negligible changes after a 90-day storage at 4 °C (Figure S14), indicative of the excellent colloidal stability of NPs.

The NPs of these PQ-cored molecules show extremely weak photoluminescence (PL) that can hardly be detected, and their PL quantum yields (Φ_{PL}'s) are as low as ~0.3% (Table S2), revealing nonradiative decay is dominant in the excited relaxation process. The dilute THF solutions of these molecules barely fluoresce either, but the PL intensities are

https://doi.org/10.1021/acsnano.1c07730
ACS Nano XXXX, XXX, XXX−XXX

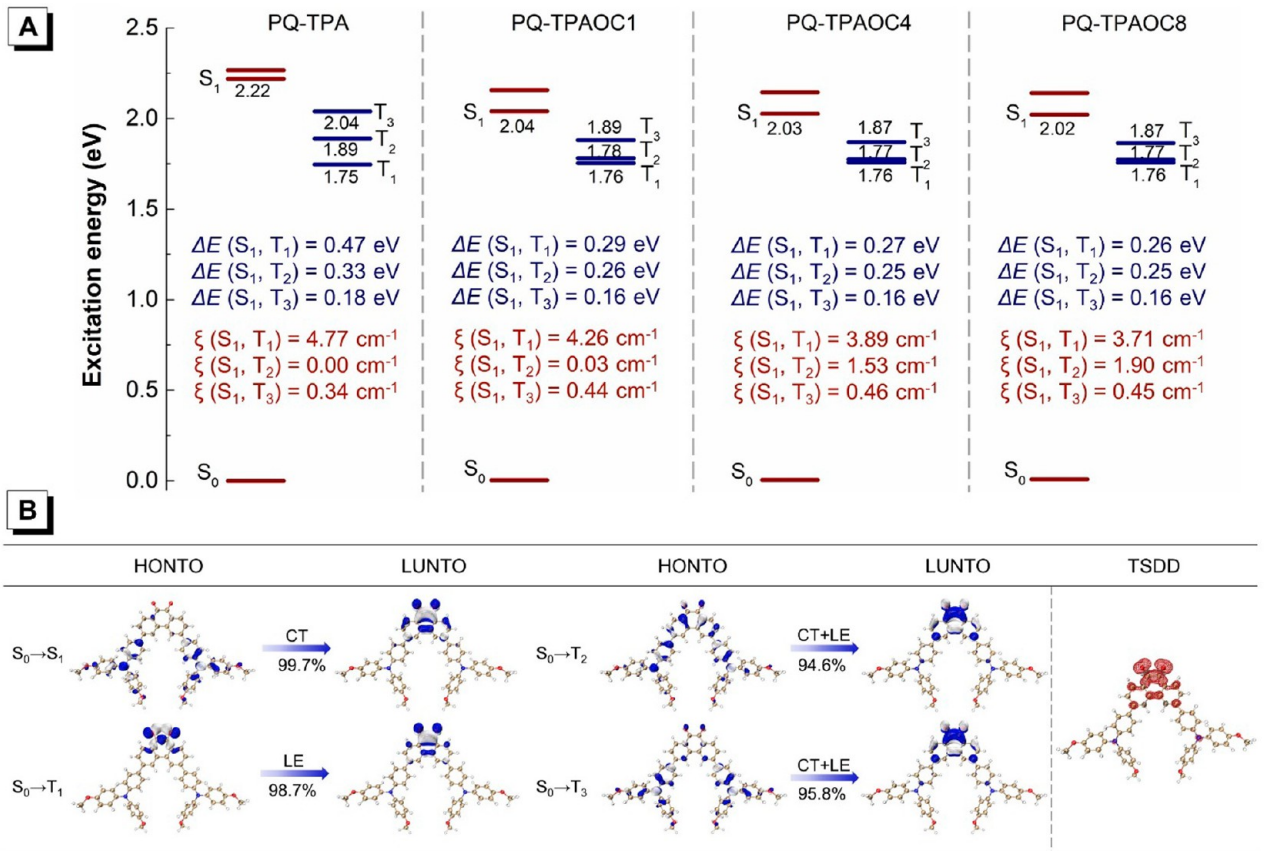

Figure 3. (A) Calculated energy gaps (ΔE) and related spin−orbit coupling constants (ξ) of PQ-TPA, PQ-TPAOC1, PQ-TPAOC4, and PQ-TPAOC8 based on S_0 structures at the level of PBE0/def2-TZVP. (B) Natural transition orbitals, eigenvalues of natural transition orbital pairs, transition characters, and spin density distributions of the T_1 states of PQ-TPAOC1.

enhanced in nonpolar toluene solutions accompanied by obvious blue shifts in the PL peaks, validating the ICT characteristics. The strong ICT effect derived from the D−A structures of these PQ-cored molecules as well as the active C═O bond stretching vibration in PQ should be responsible for the severe nonradiative decay in NPs, which conversely implies the good PDT and PTT performances.

Photothermal Performance. The photothermal performances of these NPs are subsequently assessed. As shown in Figures 2C and S15, the temperatures of all the NP solutions rise apparently upon 660 nm laser irradiation (800 mW cm^{-2}) for 300 s, with the plateau temperatures of 44.7, 79.0, 73.2, and 77.3 °C for PQ-TPA NPs, PQ-TPAOC1 NPs, PQ-TPAOC4 NPs, and PQ-TPAOC8 NPs, respectively, while the temperature of pure water exhibits negligible change, validating the photothermal effects. Based on the photothermal curves and interrelated time constants (Figure S16), the corresponding photothermal conversion efficiencies are calculated to be 21.8%, 37.1%, 27.5%, and 35.7% for PQ-TPA NPs, PQ-TPAOC1 NPs, PQ-TPAOC4 NPs, and PQ-TPAOC8 NPs, respectively.[49,50] Clearly, PQ-TPAOC1 NPs, PQ-TPAOC4 NPs, and PQ-TPAOC8 NPs exhibit higher plateau temperatures and better photothermal conversion efficiencies than PQ-TPA NPs, disclosing the presence of alkoxy chains is beneficial to photothermal performance. This is probably due to the fact that these alkoxy chains can cause loose molecular packing, which is favored for intramolecular motion. It is worth noting that these NPs also possess superior photothermal stability with steady-state temperature variation during four laser irradiation on/off cycles (Figures 2D and S17). In addition, the influence of the light source on the photothermal effect of PQ-TPAOC1 NPs is also explored. The infrared thermal images and heating−cooling curves (Figure S18) reveal that the 660 nm laser (800 mW cm^{-2}) is a suitable light source to achieve satisfactory photothermal performance, while the white light plays an insignificant role.

ROS Generation. On account of the redox cycling behaviors of the PQ-cored molecules, the toxic ROS generation capacities are evaluated by the fluorescence probing method. First, a commercial indicator, 2,7-dichlorodihydrofluorescein (DCFH), is selected to detect the total ROS involving the energy or electron transfer processes with O_2 (Figures 2E and S19).[51] When the mixtures of various NPs and DCFH are exposed to white light irradiation (50 mW cm^{-2}), the fluorescence intensities are rapidly boosted as the irradiation duration increases. In the presence of PQ-TPA NPs, PQ-TPAOC1 NPs, or PQ-TPAOC4 NPs, the emission intensities of DCFH reach nearly 400-fold enhancement after a 5 min irradiation, and their ROS generation capacities are much superior to those of commercial photosensitizers, such as crystal violet (CV) and rose bengal (RB),[52,53] under the same conditions. However, the ROS generation efficiency of PQ-TPAOC8 NPs is relatively low, probably due to the longer alkoxy chain that influences molecular aggregation; namely, the conjugated backbones of the molecules align loosely with relatively large intermolecular distances. In consequence, the ISC rate may decrease, resulting in a low concentration of triplet excitons.[54−56] Additionally, the impact of the light

https://doi.org/10.1021/acsnano.1c07730
ACS Nano XXXX, XXX, XXX−XXX

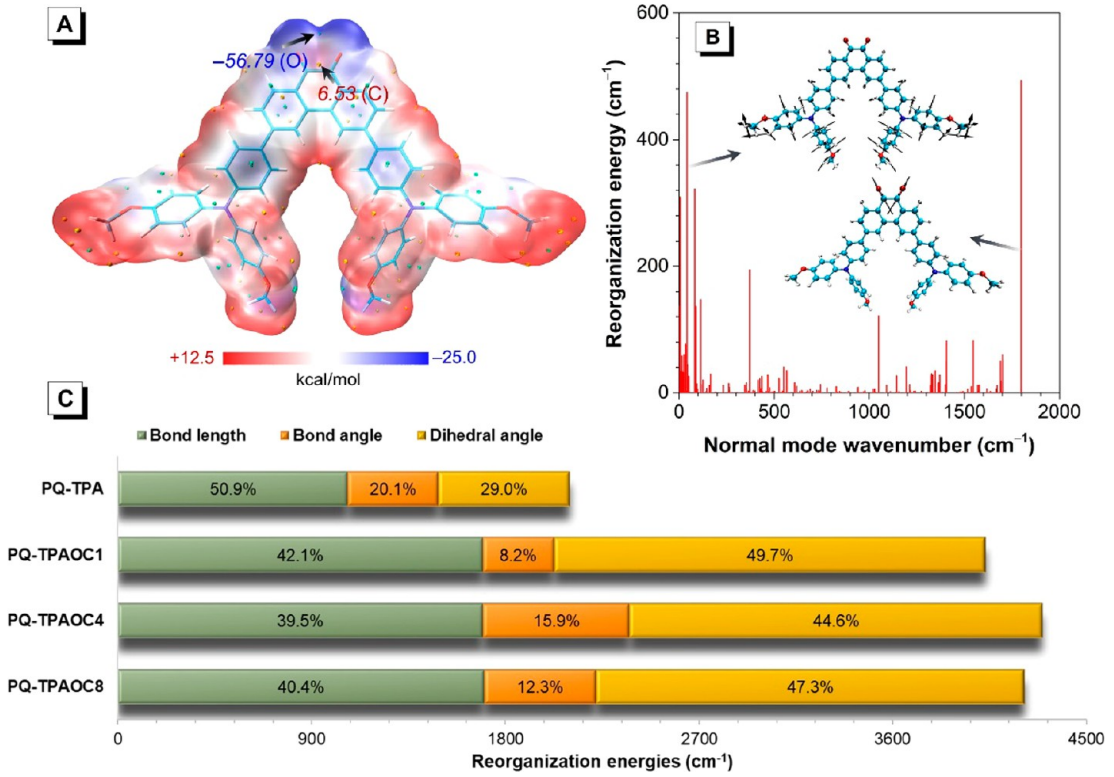

Figure 4. (A) ESP mapped molecular van der Waals surface of PQ-TPAOC1. The green and orange tiny spheres represent the surface local minima and maxima of the ESP, which are labeled by italic fonts marking both the values and the contributive atoms. (B) Calculated reorganization energies of PQ-TPAOC1 versus normal-mode frequencies. Inset: representative vibration modes. (C) Contributions to the total reorganization energy from bond length, bond angle, and dihedral angle.

source on ROS generation is further estimated based on PQ-TPAOC1 NPs that have the best comprehensive performance (Figure S20). The results indicate the combination of 660 nm laser and white light will be more effective in phototherapeutic applications.

Then, singlet oxygen ($^1O_2$) indicators, 9,10-anthracenediyl-bis(methylene) dimalonic acid (ABDA), singlet oxygen sensor green (SOSG), and HO• indicator hydroxyphenyl fluorescein (HPF) are utilized to verify the nature of the ROS generated from the NPs.[51,57] CV and RB are selected as the Type I reference and Type II reference, respectively. As illustrated in Figures 2F and G and S21 and S22, the absorbance of ABDA and the emission intensity of SOSG remain intact with these NPs under white light irradiation (50 mW cm^{-2}), which is different from the significant variation in the presence of RB NPs. These results show that these NPs can hardly generate $^1O_2$ but can yield HO• instead, as evidenced by the gradually enhanced emission intensity of HPF along with the increase of irradiation time. The capacities of HO• generation of these NPs are similar to or even better than those of CV NPs (Figures 2H and S23). Furthermore, electron spin resonance (ESR) spectroscopy using 5-*tert*-butoxycarbonyl-5-methyl-1-pyrroline-*N*-oxide (BMPO) as the spin-trap agent is adopted to monitor the generation of free radical ROS.[58,59] As shown in Figure 2I, no visible ESR signals of oxygenous radical adducts formed with BMPO can be observed in the absence of NPs or without white light irradiation. However, when the mixtures of NPs and BMPO are exposed to white light (100 mW cm^{-2}) for 5 min, obvious ESR signals can be detected. The above results unveil that the efficient ROS generation of these NPs is mainly through the Type I photochemical pathway upon light irradiation.

Photophysical and Photochemical Mechanisms. To gain an in-depth insight into the photodynamic and photothermal behaviors of these NPs, density functional theory (DFT) and time-dependent density functional theory (TD-DFT) are carried out to visualize the geometrical character and the transition properties of the PQ-cored molecules. The electronic structures of PQ-TPA, PQ-TPAOC1, PQ-TPAOC4, and PQ-TPAOC8 in the ground state (S_0) are investigated at the level of PBE0/6-31G(d,p), and the corresponding frontier molecular orbital (FMO) distributions are shown in Figure S24. The highest occupied molecular orbitals (HOMOs) are predominantly localized on the electron-donating TPA moieties, while the lowest unoccupied molecular orbitals (LUMOs) distribute mainly on the electron-withdrawing PQ core, confirming their inherent ICT effects. The full separation of FMOs gives rise to small singlet−triplet energy splitting (ΔE_{ST}) due to the decreased electron exchange energy,[60] which allows an efficient ISC process.

The subsequent TD-DFT investigations are performed on these molecules in both singlet and triplet excited states at the PBE0/def2-TZVP level to explore the essence of ROS generation. As depicted in Figure 3A, there are multiple energy transition channels from the lowest singlet excited (S_1) state to triplet states for these molecules, with a relatively small energy gap of 0.16 eV. Besides, effective spin−orbit coupling (SOC) also plays an important role in facilitating the spin-flip between singlet and triplet states. The calculated SOC values of PQ-TPA, PQ-TPAOC1, PQ-TPAOC4, and PQ-TPAOC8 between S_1 and the lowest triplet excited (T_1) states are 4.77,

https://doi.org/10.1021/acsnano.1c07730
ACS Nano XXXX, XXX, XXX−XXX

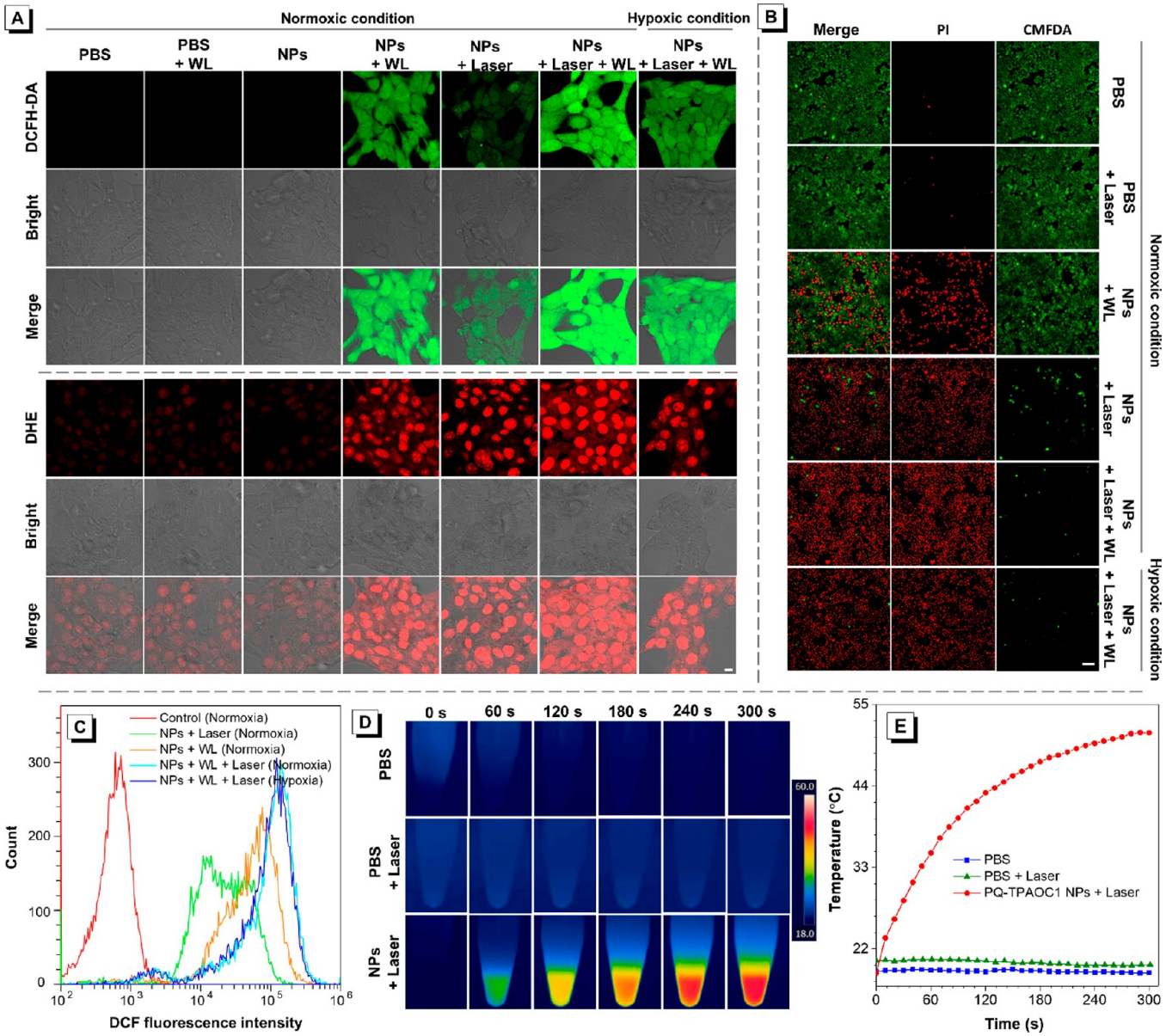

Figure 5. (A) ROS detection in 4T1 tumor cells under normoxia and hypoxia conditions using DCFH-DA and DHE as general ROS and Type I ROS fluorescence indicators, respectively, with/without white light (WL, 200 mW cm^{-2}) and/or 660 nm laser (800 mW cm^{-2}) irradiation. Scale bar = 10 μm. (B) Live/dead cell staining assays under normoxia and hypoxia conditions using CMFDA and PI as the indicators treated with PQ-TPAOC1 NPs or PBS, with/without white light (WL, 200 mW cm^{-2}) and/or 660 nm laser (800 mW cm^{-2}) irradiation. Scale bar = 100 μm. (C) Flow cytometry quantitative analysis of 4T1 cells treated with PQ-TAPOC1 NPs and DCFH-DA upon white light irradiation (200 mW cm^{-2}) and/or 660 nm laser (800 mW cm^{-2}) irradiation. (D) Infrared radiation images and (E) photothermal curves of 4T1 tumor cells under 660 nm laser irradiation (800 mW cm^{-2}) after incubation with PQ-TPAOC1 NPs (10 μg mL^{-1}) or PBS for 12 h.

4.26, 3.89, and 3.71 cm^{-1}, respectively, larger than that between S_1 and the high-lying triplet (T_2 or T_3) states. According to the natural transition orbital (NTO) analyses (Figures 3B and S25), the enhanced SOC value can be attributed to the effective mixing of the wave functions between the lowest singlet charge transfer (^{1}CT) state and the locally triplet excited (^{3}LE) state, obeying the El-Sayed rule.[61] The dense energy-level distributions with large SOC values are highly beneficial for the efficient production of a triplet state via the ISC process. Moreover, the spin density distributions of the T_1 states (TSDD) of all the molecules are concentrated on the PQ core and are almost absent on the TPA moieties. Thus, the self-annihilation of the long-lived triplet excited states, governed by the Dexter energy transfer mechanism,[62] can be suppressed by the peripheral aromatic rotors or alkoxy chains to a large degree, thereby ensuring efficient an electron transfer process with O_2 to generate Type I ROS.

According to the mechanism of the Type I ROS, these molecules at the triplet state should have effectively participated in the electron transfer process to react directly with adjacent substrates to produce radical anions, which is closely related to the high electrophilicity of the PQ core. To confirm this, the electrostatic potentials (ESPs) of these PQ-cored molecules are calculated to visually reflect the charge density distribution to speculate the reactive sites.[63−65] According to the results of ESP mapping (Figures 4A and

https://doi.org/10.1021/acsnano.1c07730
ACS Nano XXXX, XXX, XXX−XXX

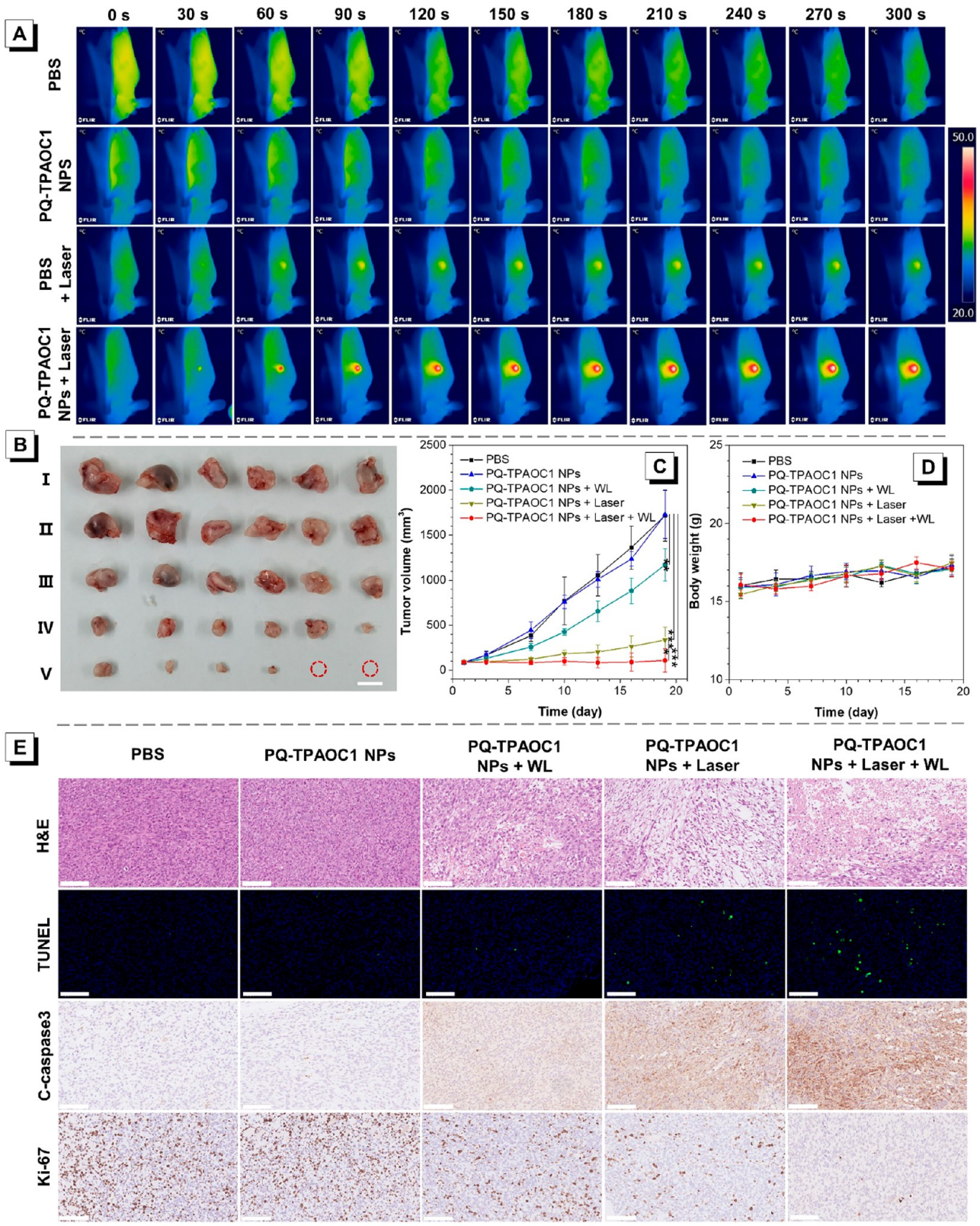

Figure 6. (A) Thermographic images of 4T1 breast tumor-bearing mice at 24 h postinjection of PQ-TPAOC1 NPs (200 μL, 1.0 mg mL^{-1}) or PBS with/without 660 nm laser irradiation (800 mW cm^{-2}). (B) Typical tumor images collected after different treatments (scale bar: 1 cm). (C) Relative tumor volume changes for various treatment groups. Data were presented as the mean ± SD (n = 6), *P < 0.05, PQ-TPAOC1 NPs + laser group vs PQ-TPAOC1 NPs + laser + WL group; **P < 0.01, PBS group vs PQ-TPAOC1 NPs + WL group; ***P < 0.001, PBS group vs PQ-TPAOC1 NPs + laser group; ***P < 0.001, PBS group vs PQ-TPAOC1 NPs + laser + WL group. (D) Body weight changes of mice with different treatments. Data were presented as the mean ± SD (n = 6). (E) H&E staining, TUNEL staining, and IHC staining of the tumor sections from mice after different treatments (scale bar: 100 μm). WL: white light of 200 mW cm^{-2};. Laser: 660 nm laser of 800 mW cm^{-2}.

https://doi.org/10.1021/acsnano.1c07730
ACS Nano XXXX, XXX, XXX−XXX

S26), the positively charged local maxima are centered on the C−C single bond between the two carbonyl groups of PQ, while the negatively charged area is mainly localized on the oxygen atoms of the carbonyl groups due to the excess lone pair electrons, which are considered as the highly reactive sites. When the PQ-cored molecule receives an external electron, the C═O double bond will be destroyed, thereby producing radical anions. And the two benzene rings attached to the quinone unit in PQ can readily stabilize the radical by forming resonance structures, providing potential Type I ROS generation ability based on the photochemical reactions.

In addition, the ESP distribution is further analyzed to predict the intermolecular interactions.[64] Obviously, the regions on both sides of the PQ core in PQ-TPA have nearly neutral potentials, which leads to the formation of relatively weak face-to-face packing in crystals (Figure S27). And the intermolecular van der Waals interactions are further visualized by the independent gradient model (IGM) analysis.[66,67] However, for PQ-TPAOC1, PQ-TPAOC4, and PQ-TPAOC8, the same regions are all colored light blue in ESP maps, which can bring forth electrostatic repulsion to hamper the occurrence of strong intermolecular $\pi-\pi$ stacking. Compared with PQ-TPA, the presence of alkoxy chain-substituted TPA in PQ-TPAOC1, PQ-TPAOC4, and PQ-TPAOC8 that has stronger electron-donating ability can facilitate the spatial isolation of molecules and also enhance the ICT effect to finally contribute to the nonradiative relaxation of the excited state, thus favoring heat production within NPs.

Furthermore, the single-molecule reorganization energies (λ) versus vibration modes are analyzed to evaluate the nonradiative decay process, and the corresponding data are shown in Figures 4 and S28 and Table S3. The total λ values of PQ-TPAOC1, PQ-TPAOC4, and PQ-TPAOC8 (over 4000 cm^{-1}) are higher than that of PQ-TPA (2099.4 cm^{-1}), which is mainly associated with the active rotation of the phenyl rings and the out-of-plane wagging vibration of the alkoxy chains. Moreover, for PQ-TPAOC1, PQ-TPAOC4, and PQ-TPAOC8, the stretching vibrations of the carbonyl groups in the high-frequency regions also play a key role in the nonradiative decay process, and about 40% of λ is contributed by bond length variation. Such kind of short-range and high-frequency bond stretching motion of the PQ core is less susceptive to the external environmental constraints and thus beneficial to achieve high photothermal conversion capacity in the aggregated state.

Synergistic PTT/Type I PDT *In Vitro*. Benefiting from the more efficient Type I ROS generation and high photothermal conversion capacity, PQ-TPAOC1 NPs are employed for *in vitro* synergistic PDT/PTT applications against mouse breast cancer 4T1 cells. The cytotoxicity of PQ-TPAOC1 NPs is quantitatively estimated by the standard cell counting kit-8 (CCK8) assay. As shown in Figure S29, the viability of 4T1 cells remains over 90% at PQ-TPAOC1 NP concentrations $\leq$40 $\mu g\ mL^{-1}$ under dark conditions, revealing excellent biocompatibility at the cellular level. Upon white light or 660 nm laser irradiation, the cells incubated with PQ-TPAOC1 NPs exhibit "turn-on" green fluorescence by using 2,7-dichlorodihydrofluorescein diacetate (DCFH-DA) as the total ROS indictor (Figure 5A). A brighter green fluorescence signal can be observed by using both white light and 660 nm laser as the illumination source, indicating the dual light sources can furnish better PDT efficacy. Meanwhile, the selective fluorescent probe dihydroethidium (DHE) for free radical ROS indicates an apparent increase of signal intensity in the simultaneous presence of PQ-TPAOC1 NPs and light irradiation, demonstrating the intracellular Type I ROS production, which is in good agreement with the results in aqueous media discussed above.[68,69] In addition, the two fluorescence probes are further used to monitor the intracellular ROS generation of PQ-TPAOC1 NPs under hypoxia condition with both white light and 660 nm laser irradiation. The PQ-TPAOC1 NPs can still achieve an excellent PDT effect even under hypoxia condition (Figure 5A), indicating the Type I ROS produced by PQ-TPAOC1 NPs will be advantageous against tumor hypoxia. The results are in accordance with the flow cytometric analysis, which displays nearly overlapped fluorescence intensity curves of hypoxia cells and normoxia cells (Figure 5C). Moreover, the PTT efficacy *in vitro* of PQ-TPAOC1 NPs is further evaluated. As displayed in Figure 5D and E, after a 12 h incubation of 4T1 cells with PQ-TPAOC1 NPs, the intracellular temperature rises rapidly upon 660 nm laser irradiation (800 mW cm^{-2}), reaching a plateau at 51.2 °C for 5 min. The results reveal the outstanding synergistic PTT/Type I PDT efficacy of PQ-TPAOC1 NPs *in vitro*. To further detect the comprehensive phototherapeutic performance of PQ-TPAOC1 NPs intuitively, the 5-chloromethylfluorescein diacetate/propidium iodide (CMFDA/PI) staining strategy is utilized to distinguish the living and dead cancer cells (Figure 5B). As expected, almost all the 4T1 cells present the death state with brighter red fluorescence signals in the presence of PQ-TPAOC1 NPs upon 660 nm laser irradiation with/without white light, in comparison with the single PDT pathway under white light irradiation (200 mW cm^{-2}). Therefore, the highly efficient PTT/Type I PDT combination can indeed significantly improve the phototherapeutic efficacy.

Synergistic PTT/Type I PDT *In Vivo*. The *in vivo* synergistic PTT/Type I PDT of PQ-TPAOC1 NPs is then investigated by employing the subcutaneous xenograft 4T1 breast tumor-bearing mouse model. Hemolysis tests are carried out to assess the hemocompatibility of PQ-TPAOC1 NPs (Figure S30). Negligible hemolysis occurs in the PQ-TPAOC1 NPs group as well as PBS and DSPE-mPEG2000, disclosing that PQ-TPAOC1 NPs are appropriate for intravenous injection. To monitor the *in vivo* distribution and tumor accumulation of nanoparticles, the TB/PQ-TPAOC1@DSPE-mPEG2000 NPs containing red fluorescent TB[70] with aggregation-induced emission property for fluorescence imaging are further prepared. As shown in Figure S31, the fluorescence intensity in the tumor site reaches the maximum level after intravenous injection of NPs for 24 h. And the tumor tissues exhibit a significantly stronger fluorescence signal than any other organs, indicating the effectively preferential accumulation of NPs in tumors with reduced side effects. Subsequently, the *in vivo* phototherapeutic study of PQ-TPAOC1 NPs is conducted.

After injecting PQ-TPAOC1 NPs or PBS into the 4T1 tumor-bearing mice via the tail vein, the tumor region temperature is recorded with/without 660 nm laser irradiation. The infrared thermal images and photothermal curves display that the temperature at the tumor site increases with the extension of laser irradiation time in the PQ-TPAOC1 NP-treated group and can facilely reach 54.9 °C after a 660 nm laser irradiation (800 W cm^{-2}) for 5 min (Figures 6A and S32). This is mainly attributed to the targeting accumulation in

https://doi.org/10.1021/acsnano.1c07730
ACS Nano XXXX, XXX, XXX−XXX

tumors and the outstanding photothermal performance of PQ-TPAOC1 NPs. To further comprehensively evaluate the combination antitumor efficacy of PQ-TPAOC1 NPs over a 19-day follow-up period, the tumor-bearing mice are randomly divided into the following treatment groups (n = 6): (I) PBS; (II) PQ-TPAOC1 NPs; (III) PQ-TPAOC1 NPs + white light; (IV) PQ-TPAOC1 NPs + 660 nm laser; and (V) PQ-TPAOC1 NPs + 660 nm laser + white light. The tumor volumes are respectively recorded during the 19-day treatment period (Figure 6B and C). In groups I and II, the tumor volumes increase rapidly without light irradiation. The similar tumor growth kinetics indicate that PQ-TPAOC1 NPs themselves have a negligible antitumor effect. By contrast, the PQ-TPAOC1 NP-treated group inhibits tumor growth appropriately in the presence of white light irradiation with a tumor inhibition rate of 31.9%, which only involves the PDT pathway. A better therapeutic efficacy in group IV can be observed for the smaller tumor growth with only about 3.7-fold enhancement in volume on day 19, leading to a higher tumor inhibition rate of 80.4%. Notably, the "PQ-TPAOC1 NPs + 660 nm laser + white light" treatment holds the best antitumor effect with the highest tumor inhibition rate of 93.7% and the tumors in some mice are even completely ablated after a 19-day PTT/Type I PDT synergistic treatment.

The antitumor effect of each treatment group is further assessed by histological and immunohistochemical analyses. As presented in Figure 6E, the hematoxylin and eosin (H&E) staining of tumor slices clearly reveals the extensive destruction of tumor tissues after synergistic treatment of PQ-TPAOC1 NPs and light irradiation, whereas the tumor cells arrange densely with normal morphology in the control group. Moreover, the excellent antitumor efficacy of PQ-TPAOC1 NP-mediated PTT/Type I PDT is further validated by the terminal deoxynucleotidyl transferase dUTP nick end labeling (TUNEL) staining, and the density of positive cells (green fluorescence) is noticeably highest in group V. The findings from TUNEL assay are well consistent with cell apoptosis levels as indicated by the high expression of apoptosis executioner cleaved-caspase3 (C-caspase3) gene. The proliferation marker, Ki-67, also proves that the treatment of "PQ-TPAOC1 NPs + 660 nm laser + white light" is the most efficacious way to induce the apoptosis and suppress the proliferation activity of tumor cells. Additionally, the side toxic effects in all treatments are also evaluated by monitoring the body weights of mice and histological analysis of the major organs. As shown in Figure 6D, the body weights of mice from these five groups enhance slowly during treatment, suggesting the negligible acute toxicity in *in vivo* applications. The H&E-stained slices of the major organs (lung, liver, spleen, kidney, and heart) of the treated mice after 19 days indicate that there are no noticeable tissue damage and inflammatory lesions toward these organs (Figure S33), further demonstrating the excellent biological safety of PQ-TPAOC1 NP-mediated synergistic PTT/Type I PDT *in vivo*.

CONCLUSION

In summary, a series of phototheranostic agents consisting of an electron-withdrawing PQ core and electron-donating TPA derivatives are designed and synthesized. Based on the PQ core and subtle structural tuning, highly efficient Type I ROS generation and outstanding photothermal conversion capacity can be simultaneously achieved in the NPs fabricated by these PQ-cored molecules. The experimental and theoretical studies disclose that the specific redox cycling behavior, facilitated ISC process, and active intramolecular bond stretching vibration of the PQ core collectively lead to the outstanding synergistic Type I photodynamic and photothermal effects of the NPs. Both the *in vitro* and *in vivo* experiments further confirm that PQ-TPAOC1 NPs with excellent biocompatibility hold impressive antitumor therapy efficacy upon white light and 660 nm laser irradiation, and the combination therapy indeed can significantly induce the apoptosis and inhibit the proliferation of tumor cells. However, the penetration depth still remains limited at present. The development of high-performance near-infrared PTT/Type I PDT nanoagents to augment the treatment efficacy of deep-seated tumors could be an important direction in the future.

EXPERIMENTAL SECTION

Preparation of Nanoparticles. Two milliliters of THF solution containing 2 mg of PQ-TPA, PQ-TPAOC1, PQ-TPAOC4, PQ-TPAOC8, CV, or RB and 4 mg of DSPE-mPEG2000 was poured into 10 mL of deionized water, followed by sonication for 20 min. The residue THF solvent was evaporated by violently stirring the suspension in a fume hood for 24 h, and a colloidal solution was obtained. The TB/PQ-TPAOC1@DSPE-mPEG2000 NPs containing PQ-TPAOC1 (1 mg), TB (1 mg), and amphiphilic DSPE-mPEG2000 (4 mg) were prepared by the same nanoprecipitation method. The resulting nanoparticle suspension was filtered with a 0.2 μm syringe-driven filter for *in vitro* and *in vivo* experiments (Millipore). The encapsulation efficiency of PQ-TPAOC1 NPs is further calculated. First, lyophilized PQ-TPAOC1 NPs were dissolved in THF to extract PQ-TPAOC1 into THF. Subsequently, the obtained solution was analyzed by a UV−vis spectrophotometer at 545 nm, and the PQ-TPAOC1-encapsulation content was determined using a calibration curve. Finally, the encapsulation efficiency (EE) was calculated using the following equations: EE (%) = $[B/A] \times 100\%$, in which A is the total weight of PQ-TPAOC1 used, and B is the weight of PQ-TPAOC1 found in the particles.

Reactive Oxygen Species (ROS) Detection. *General ROS Detection.* The fluorescent probe 2,7-dichlorodihydrofluorescein (DCFH) was applied as the indicator to detect the general ROS generation, which was converted from DCFH-DA (0.5 mL, 1 mM in ethanol) reacting with an aqueous solution of NaOH (2 mL, 10 mM) for 30 min at room temperature. The hydrolysate was then neutralized with 10 mL of PBS buffer solution to get the stock solution with a concentration of 40 μM. PBS buffer solution containing 1 μM DCFH was mixed separately with different samples (PQ-TPA NPs, PQ-TPAOC1 NPs, PQ-TPAOC4 NPs, PQ-TPAOC8 NPs, CV NPs, and RB NPs), and the final concentrations were 1 μM. Then the mixture was irradiated with white light (50 mW cm^{-2} or 200 mW cm^{-2}) and/or 660 nm laser irradiation (800 mW cm^{-2}). The fluorescence intensity at 522 nm was recorded (excitation wavelength is 488 nm).

Singlet Oxygen ($^1O_2$) Detection. Singlet Oxygen Sensor Green (SOSG) and 9,10-anthracenediyl-bis(methylene) dimalonic acid (ABDA) were applied as the indicators to detect the $^1O_2$ generation. PBS buffer solution containing 5 μM SOSG (stock solution: 5 mM in DMSO) was mixed separately with different samples (PQ-TPA NPs, PQ-TPAOC1 NPs, PQ-TPAOC4 NPs, PQ-TPAOC8 NPs, and RB NPs), and the final concentrations were 1 μM. Then the fluorescence intensity at 530 nm was recorded (excitation wavelength was 480 nm) after the mixture was irradiated with white light (50 mW cm^{-2}). PBS buffer solution containing 30 μM ABDA (stock solution: 30 mM in DMSO) was mixed separately with different samples (PQ-TPA NPs, PQ-TPAOC1 NPs, PQ-TPAOC4 NPs, PQ-TPAOC8 NPs, and RB NPs), and the final concentrations were 1 μM. Then the absorbance of ABDA at 380 nm was recorded after the mixture was irradiated with white light (50 mW cm^{-2}).

Hydroxyl Radical (HO•) Detection. The fluorescent probe hydroxyphenyl fluorescein (HPF) was applied as the indicator to

https://doi.org/10.1021/acsnano.1c07730
ACS Nano XXXX, XXX, XXX−XXX

detect the HO• generation. PBS buffer solution containing 5 μM HPF (stock solution: 5 mM in DMF) was mixed separately with different samples (PQ-TPA NPs, PQ-TPAOC1 NPs, PQ-TPAOC4 NPs, PQ-TPAOC8 NPs, and CV NPs), and the final concentrations were 1 μM. Then the fluorescence intensity at 514 nm was recorded (excitation wavelength is 480 nm) after the mixture was irradiated with white light (50 mW cm^{-2}).

Type I ROS Detection by ESR Spectroscopy. 5-*tert*-Butoxycarbonyl-5-methyl-1-pyrroline-*N*-oxide (BMPO) was employed as spin-trapping agent to detect the generation of Type I ROS. PBS buffer solution containing 25 mM BMPO was mixed separately with 10 μM PQ-TPA, PQ-TPAOC1, PQ-TPAOC4, and PQ-TPAOC8. The ESR spectra were recorded after the mixture was irradiated with white light (100 mW cm^{-2}) for 5 min. And the mixture without white light irradiation and pure BMPO solution were tested as controls.

Photothermal Performance. The aqueous solutions of PQ-TPA NPs, PQ-TPAOC4 NPs, and PQ-TPAOC8 NPs (100 μL, 150 μM) were continuously exposed to 660 nm laser irradiation with the power density of 800 mW cm^{-2} for 5 min. And the PQ-TPAOC1 NP aqueous solutions were treated with 660 nm laser irradiation (800 mW cm^{-2}) and/or white light (200 mW cm^{-2}). At the same time, the temperature changes of the solutions were monitored. The corresponding IR thermal images of the sample tubes were also recorded using a FLIR E6 camera and quantified by FLIR Examiner software. To further evaluate the photothermal stability, the PQ-TPA NPs, PQ-TPAOC1 NPs, PQ-TPAOC4 NPs, and PQ-TPAOC8 NPs were treated with 660 nm laser irradiation (800 mW cm^{-2}) for 300 s; then the laser was removed to cool for 300 s, and the irradiation on−off cycles were repeated four times. In addition, the photothermal conversion efficiency (η) of NPs was calculated according to the equation from the previous report.[49,50]

$$\eta = \frac{hs(T_{max} - T_{surr}) - Q_{dis}}{I(1 - 10^{-A_\lambda})}$$

$$\theta = \frac{T - T_{surr}}{T_{max} - T_{surr}} \qquad dt = -\frac{\sum_i m_i C_{p,i}}{hs}\frac{d\theta}{\theta}$$

$$t = -\frac{\sum_i m_i C_{p,i}}{hs}\theta$$

where hs can be obtained by using the linear time data of the cooling period vs $-\ln\theta$. T_{max} is the temperature change of the aqueous solution of NPs at the maximum steady-state temperature, and T_{surr} is the ambient temperature of the surroundings. I is the laser power used for the photothermal experiment, and A_λ is the absorbance of NPs at the wavelength of the laser. Q_{dis} expresses the heat associated with the light absorption by solvent, and m and C_p are the mass and heat capacity of water used as solvent. Thus, the photothermal conversion efficiency (PCE, η) of NPs can be calculated.

Photostability. The aqueous solutions of PQ-TPA NPs, PQ-TPAOC1 NPs, PQ-TPAOC4 NPs, and PQ-TPAOC8 NPs (0.1 mg mL^{-1}) were irradiated by 660 nm laser irradiation (800 mW cm^{-2}) and/or white light (200 mW cm^{-2}) for 0, 1, 2, 3, 4, and 5 min, respectively, and the PQ-TPAOC1 NPs were also stored at 4 °C for 90 days. The corresponding UV−vis absorption spectra and average diameters of NPs in different states were measured.

Cell Culture and Cytotoxicity Assessment. 4T1 cells (mouse breast cancer cells) were purchased from Procell (Wuhan, China), and were cultured in Roswell Park Memorial Institute (RPMI) 1640 medium containing 10% fetal bovine serum and 1% 100 U/mL antibiotics (penicillin, streptomycin). The culture condition was 37 °C, witih the cell culture incubator containing 5% CO_2 for culture. Before experiments, the cells were precultured until the confluence was reached. The CCK8 assay was used to assess the cytotoxicity of PQ-TPAOC1 NPs against 4T1 cancer cells. Briefly, the 4T1 cancer cells were inoculated in a 96-well plate with a cell density of 5×10^4 cells mL^{-1}. After 24 h of culture, the 4T1 cancer cells were exposed to a series of different concentrations of PQ-TPAOC1 NPs. At 24 h postaddition of NPs, the cells were washed with 1× PBS buffer. Then 10 μL of newly prepared CCK8 solution was added to each well. After incubation in the incubator for 2 h, the enzymatic standard reads the absorbance value of cells at 450 nm.

***In Vitro* PDT Application.** *Cellular Uptake and Intracellular ROS Detection.* 4T1 cells (1,000) were incubated with PQ-TPAOC1 NPs (10 μg mL^{-1}) in a confocal dish for 12 h, and some 4T1 cells were incubated under hypoxia conditions for 12 h. These samples were further incubated with DCFH-DA (10 μM) or dihydroethidium (DHE, 5 μM) for another 60 min and washed with PBS three times (1 mL). They were irradiated by white light (200 mW cm^{-2}) and/or a 660 nm laser (800 mW cm^{-2}) for 5 min. As the control group, cells were incubated with PBS in confocal dishes. Fluorescence images were recorded on a confocal laser scanning microscope (CLSM) (Zeiss LSM 880). The samples incubated with DCFH-DA under irradiation were excited with a 488 nm laser, and the fluorescence was collected from 520 to 560 nm. The samples incubated with DHE under irradiation were excited with a 488 nm laser, and the fluorescence was collected from 590 to 630 nm.

In Vitro PTT Application. 4T1 cells were incubated with PQ-TPAOC1 NPs (10 μg mL^{-1}) in a confocal dish for 12 h. The cells were treated by trypsin elimination, and PQ-TPAOC1-treated 4T1 cells were obtained by centrifugation. The cell precipitate located at the bottom of the EP tube receives laser irradiation (800 mW cm^{-2}) for 5 min while the IR thermal camera records the temperature change at the bottom of the tube.

Live/Dead Cell Staining Assay. All treated cells were incubated with CMFDA and PI to trace the living and dead cells. Briefly, 4T1 cells were first incubated with CMFDA (5 μM) for 60 min. Then the cells were washed with PBS 3 times and incubated with PI (2 μM) for 20 min. The cells were visualized under the CLSM (Zeiss LSM 880).

Flow Cytometric Analysis. After incubation of 4T1 cells with nanoparticles for 12 h under normoxia or hypoxia conditions, the supernatant was removed and washed 3 times with PBS. Subsequently, the cells were incubated with ROS indicator (DCFH-DA) for 30 min and illuminated with white light (200 mW cm^{-2}) and/or a 660 nm laser (800 mW cm^{-2}). Immediately thereafter, the cells were separated from the culture dish with trypsin, and then flow cytometry was performed. The cells were resuspended in 100 μL of FACS buffer and then analyzed by flow cytometry (Beckman, cytoflex S).

Hemolysis Assay. The hemolytic activity of the nanoparticles was assessed by spectrophotometry. 0.5 mL of erythrocyte suspension was mixed with 0.5 mL of the substance under test, such as distilled water, PBS, DSPE-mPEG2000, or PQ-TPAOC1 NPs. The two were mixed and incubated at 37 °C for 3 h before centrifugation to remove the erythrocytes. The absorbance of the supernatant was measured at 540 nm using a UV−vis spectrophotometer, and the hemolytic activity of distilled water was defined as 100%.

Animal Models. All animal studies were approved by the Animal Ethics Committee in Tongji Hospital, Tongji Medical College, Huazhong University of Science and Technology. Six-week-old female BALB/c mice were purchased from Beijing Vital River Laboratory Animal Technology Co. Ltd. (Beijing, China). All mice were fed with sufficient food and water in a room with 26 °C and 12−12 h of darkness and daytime circulation. The tumor volume was measured by caliper and calculated as follows: volume = (tumor length) × (tumor width)^2/2.

In Vivo Photothermal Imaging. 4T1 tumor-bearing mice were used to confirm the photothermal effect of PQ-TPAOC1 NPs. When the tumor grew to ~300 mm^3, 200 μL of PQ-TPAOC1 NPs (1 mg mL^{-1}) was injected into the mice through the tail vein. After 24 h of injection, the tumor was irradiated by a 660 nm laser (800 mW cm^{-2}) for 5 min. The changes of tumor temperature were recorded by an IR thermal camera (Fluke Shanghai Inc.).

In Vivo Phototherapeutic Study. 4T1 tumor-bearing mice were used to confirm the phototherapeutic effect of PQ-TPAOC1 NPs. Briefly, the growth curve of the 4T1 tumor was recorded when it reached 60 mm^3, and the treatment was started when the tumor volume reached about 100 mm^3. 200 μL of PQ-TPAOC1 NPs (1 mg mL^{-1}) was injected into the mice through the tail vein. After 24 h of

https://doi.org/10.1021/acsnano.1c07730
ACS Nano XXXX, XXX, XXX−XXX

injection, the tumor was irradiated by a 660 nm laser (800 mW cm^{-2}, 5 min) or white light (200 mW cm^{-2}, 10 min). For the PQ-TPAOC1 NPs + laser + WL group, in addition to receiving laser irradiation, and after 24 h, it also needed to receive white light irradiation (200 mW cm^{-2}, 10 min). Tumor volumes of mice were monitored.

Histology Examination. Tumors and organs were harvested right after mice were sacrificed, fixed in 10% neutral buffered formalin for 24 h, processed into paraffin, sectioned into slices, and stained with hematoxylin and eosin (H&E) for examination by a digital microscope.

TUNEL Staining. TUNEL staining was performed to detect apoptotic cells using a TUNEL BrightGreen Apoptosis Detection Kit (Vazyme) according to the manufacturer's protocol.

Immunohistochemical Staining. Briefly, after slides were dewaxed, hydrated, antigen repaired, and closed with BSA, etc., primary antibodies (Ki-67 and C-caspase3) were incubated overnight at 4 °C. The following day, slides were washed in PBS for 5 min and incubated with horseradish peroxidase-labeled secondary antibody in 37 °C. Finally, immunoreactivity was performed with 3,3′-diaminobenzidine as a chromogenic agent and hematoxylin was restained.

ASSOCIATED CONTENT

Supporting Information

The Supporting Information is available free of charge at https://pubs.acs.org/doi/10.1021/acsnano.1c07730.

General information, synthesis and characterization, crystal data, cyclic voltammograms, photophysical properties, theoretical calculation data, and *in vitro* and *in vivo* experimental data (PDF)

X-ray crystallographic data for PQ-TPA (CIF)

AUTHOR INFORMATION

Corresponding Author

Zujin Zhao − *State Key Laboratory of Luminescent Materials and Devices, Guangdong Provincial Key Laboratory of Luminescence from Molecular Aggregates, South China University of Technology, Guangzhou 510640, China;* orcid.org/0000-0002-0618-6024; Email: mszjzhao@scut.edu.cn

Authors

Jingjing Guo − *State Key Laboratory of Luminescent Materials and Devices, Guangdong Provincial Key Laboratory of Luminescence from Molecular Aggregates, South China University of Technology, Guangzhou 510640, China*

Jun Dai − *Department of Obstetrics and Gynecology, Tongji Hospital, Tongji Medical College, Huazhong University of Science and Technology, Wuhan 430074, China*

Xiaoluo Peng − *State Key Laboratory of Luminescent Materials and Devices, Guangdong Provincial Key Laboratory of Luminescence from Molecular Aggregates, South China University of Technology, Guangzhou 510640, China*

Quan Wang − *Engineering Research Center of Nano-Geomaterials of Ministry of Education, Faculty of Materials Science and Chemistry, China University of Geosciences, Wuhan 430074, China*

Shixuan Wang − *Department of Obstetrics and Gynecology, Tongji Hospital, Tongji Medical College, Huazhong University of Science and Technology, Wuhan 430074, China*

Xiaoding Lou − *Engineering Research Center of Nano-Geomaterials of Ministry of Education, Faculty of Materials Science and Chemistry, China University of Geosciences, Wuhan 430074, China;* orcid.org/0000-0002-6556-2034

Fan Xia − *Engineering Research Center of Nano-Geomaterials of Ministry of Education, Faculty of Materials Science and Chemistry, China University of Geosciences, Wuhan 430074, China;* orcid.org/0000-0001-7705-4638

Ben Zhong Tang − *State Key Laboratory of Luminescent Materials and Devices, Guangdong Provincial Key Laboratory of Luminescence from Molecular Aggregates, South China University of Technology, Guangzhou 510640, China; Shenzhen Institute of Aggregate Science and Technology, School of Science and Engineering, The Chinese University of Hong Kong, Guangdong 518172, China; AIE Institute, Guangzhou Development District, 510530 Guangzhou, China;* orcid.org/0000-0002-0293-964X

Complete contact information is available at: https://pubs.acs.org/10.1021/acsnano.1c07730

Author Contributions

[∇]The manuscript was written through contributions of all authors. All authors have given approval to the final version of the manuscript. J.G. and J.D. contributed equally to this work.

Notes

The authors declare no competing financial interest.

ACKNOWLEDGMENTS

This research was financially supported by the National Natural Science Foundation of China (21788102, 21874121, and 21974128), Natural Science Foundation of Guangdong Province (2019B030301003), and the Fundamental Research Funds for the Central Universities.

REFERENCES

(1) Ng, K. K.; Zheng, G. Molecular Interactions in Organic Nanoparticles for Phototheranostic Applications. *Chem. Rev.* **2015**, *115*, 11012−11042.

(2) Qi, J.; Ou, H.; Liu, Q.; Ding, D. Gathering Brings Strength: How Organic Aggregates Boost Disease Phototheranostics. *Aggregate* **2021**, *2*, 95−113.

(3) Yang, Z.; Chen, X. Semiconducting Perylene Diimide Nanostructure: Multifunctional Phototheranostic Nanoplatform. *Acc. Chem. Res.* **2019**, *52*, 1245−1254.

(4) Cheng, L.; Wang, C.; Feng, L.; Yang, K.; Liu, Z. Functional Nanomaterials for Phototherapies of Cancer. *Chem. Rev.* **2014**, *114*, 10869−10939.

(5) Dai, J.; Wu, X.; Ding, S.; Lou, X.; Xia, F.; Wang, S.; Hong, Y. Aggregation-Induced Emission Photosensitizers: From Molecular Design to Photodynamic Therapy. *J. Med. Chem.* **2020**, *63*, 1996−2012.

(6) Feng, G.; Zhang, G. Q.; Ding, D. Design of Superior Phototheranostic Agents Guided by Jablonski Diagrams. *Chem. Soc. Rev.* **2020**, *49*, 8179−8234.

(7) Huang, X.; Yin, Y.; Wu, M.; Zan, W.; Yang, Q. LyP-1 Peptide-Functionalized Gold Nanoprisms for SERRS Imaging and Tumor Growth Suppressing by PTT Induced-Hyperthermia. *Chin. Chem. Lett.* **2019**, *30*, 1335−1340.

(8) Shi, M.; Fu, Z.; Pan, W.; Chen, Y.; Wang, K.; Zhou, P.; Li, N.; Tang, B. A Protein-Binding Molecular Photothermal Agent for Tumor Ablation. *Angew. Chem., Int. Ed.* **2021**, *60*, 13564−13568.

(9) Zhao, Z.; Chen, C.; Wu, W.; Wang, F.; Du, L.; Zhang, X.; Xiong, Y.; He, X.; Cai, Y.; Kwok, R. T. K.; Lam, J. W. Y.; Gao, X.; Sun, P.; Phillips, D. L.; Ding, D.; Tang, B. Z. Highly Efficient Photothermal Nanoagent Achieved by Harvesting Energy *via* Excited-State Intramolecular Motion within Nanoparticles. *Nat. Commun.* **2019**, *10*, 768.

(10) Dai, J.; Li, Y.; Long, Z.; Jiang, R.; Zhuang, Z.; Wang, Z.; Zhao, Z.; Lou, X.; Xia, F.; Tang, B. Z. Efficient Near-Infrared Photosensitizer with Aggregation-Induced Emission for Imaging-Guided Photodynamic Therapy in Multiple Xenograft Tumor Models. *ACS Nano* **2020**, *14*, 854−866.
(11) Nita, M.; Grzybowski, A. The Role of the Reactive Oxygen Species and Oxidative Stress in the Pathomechanism of the Age-Related Ocular Diseases and Other Pathologies of the Anterior and Posterior Eye Segments in Adults. *Oxid. Med. Cell. Longevity* **2016**, *2016*, 3164734.
(12) Dai, J.; Wu, M.; Wang, Q.; Ding, S.; Dong, X.; Xue, L.; Zhu, Q.; Zhou, J.; Xia, F.; Wang, S.; Hong, Y. Red Blood Cell Membrane-Camouflaged Nanoparticles Loaded with AIEgen and Poly(I:C)for Enhanced Tumoral Photodynamic -Immunotherapy. *Natl. .Sci. .Rev. .* **2021**, *8*, nwab039.
(13) Cheng, H.; Zhu, J.-Y.; Li, S.-Y.; Zeng, J.-Y.; Lei, Q.; Chen, K.-W.; Zhang, C.; Zhang, X.-Z. An O_2 Self-Sufficient Biomimetic Nanoplatform for Highly Specific and Efficient Photodynamic Therapy. *Adv. Funct. Mater.* **2016**, *26*, 7847−7860.
(14) Dang, J.; He, H.; Chen, D.; Yin, L. Manipulating Tumor Hypoxia toward Enhanced Photodynamic Therapy (PDT). *Biomater. Sci.* **2017**, *5*, 1500−1511.
(15) Sun, Y.; Zhao, D.; Wang, G.; Wang, Y.; Cao, L.; Sun, J.; Jiang, Q.; He, Z. Recent Progress of Hypoxia-Modulated Multifunctional Nanomedicines to Enhance Photodynamic Therapy: Opportunities, Challenges, and Future Development. *Acta Pharm. Sin. B* **2020**, *10*, 1382−1396.
(16) Camporesi, E. M. Side Effects of Hyperbaric Oxygen Therapy. *Undersea Hyperb. Med.* **2014**, *41*, 253−257.
(17) Fan, W.; Huang, P.; Chen, X. Overcoming the Achilles' Heel of Photodynamic Therapy. *Chem. Soc. Rev.* **2016**, *45*, 6488−6519.
(18) Li, M.; Xia, J.; Tian, R.; Wang, J.; Fan, J.; Du, J.; Long, S.; Song, X.; Foley, J. W.; Peng, X. Near-Infrared Light-Initiated Molecular Superoxide Radical Generator: Rejuvenating Photodynamic Therapy against Hypoxic Tumors. *J. Am. Chem. Soc.* **2018**, *140*, 14851−14859.
(19) Wan, Q.; Zhang, R.; Zhuang, Z.; Li, Y.; Huang, Y.; Wang, Z.; Zhang, W.; Hou, J.; Tang, B. Z. Molecular Engineering to Boost AIE-Active Free Radical Photogenerators and Enable High-Performance Photodynamic Therapy under Hypoxia. *Adv. Funct. Mater.* **2020**, *30*, 2002057.
(20) Zhuang, Z.; Dai, J.; Yu, M.; Li, J.; Shen, C.; Hu, R.; Lou, X.; Zhao, Z.; Tang, B. Z. Type I Photosensitizers Based on Phosphindole Oxide for Photodynamic Therapy: Apoptosis and Autophagy Induced by Endoplasmic Reticulum Stress. *Chem. Sci.* **2020**, *11*, 3405−3417.
(21) Fan, W.; Yung, B.; Huang, P.; Chen, X. Nanotechnology for Multimodal Synergistic Cancer Therapy. *Chem. Rev.* **2017**, *117*, 13566−13638.
(22) Tian, B.; Wang, C.; Zhang, S.; Feng, L.; Liu, Z. Photothermally Enhanced Photodynamic Therapy Delivered by Nano-Graphene Oxide. *ACS Nano* **2011**, *5*, 7000−7009.
(23) Kwon, N.; Kim, H.; Li, X. S.; Yoon, J. Supramolecular Agents for Combination of Photodynamic Therapy and Other Treatments. *Chem. Sci.* **2021**, *12*, 7248−7268.
(24) Lv, K.; Lin, H.; Qu, F. Biodegradable Hollow Co_3S_4@N-Doped Carbon as Enhanced PTT/PDT Agent for Multimodal MR/Thermal Imaging and Synergistic Antitumor Therapy. *Chem. Eng. J.* **2020**, *392*, 124555.
(25) Yan, S.; Zeng, X.; Tang, Y.; Liu, B. F.; Wang, Y.; Liu, X. Activating Antitumor Immunity and Antimetastatic Effect through Polydopamine-Encapsulated Core-Shell Upconversion Nanoparticles. *Adv. Mater.* **2019**, *31*, No. e1905825.
(26) Jiang, R.; Dai, J.; Dong, X.; Wang, Q.; Meng, Z.; Guo, J.; Yu, Y.; Wang, S.; Xia, F.; Zhao, Z.; Lou, X.; Tang, B. Z. Improving Image-Guided Surgical and Immunological Tumor Treatment Efficacy by Photothermal and Photodynamic Therapies Based on a Multifunctional NIR AIEgen. *Adv. Mater.* **2021**, *33*, 2101158.
(27) Wang, D.; Lee, M. M. S.; Xu, W.; Shan, G.; Zheng, X.; Kwok, R. T. K.; Lam, J. W. Y.; Hu, X.; Tang, B. Z. Boosting Non-Radiative Decay to Do Useful Work: Development of a Multi-Modality Theranostic System from an AIEgen. *Angew. Chem., Int. Ed.* **2019**, *58*, 5628−5632.
(28) Xu, W.; Zhang, Z.; Kang, M.; Guo, H.; Li, Y.; Wen, H.; Lee, M. M. S.; Wang, Z.; Kwok, R. T. K.; Lam, J. W. Y.; Li, K.; Xi, L.; Chen, S.; Wang, D.; Tang, B. Z. Making the Best Use of Excited-State Energy: Multimodality Theranostic Systems Based on Second Near-Infrared (NIR-II) Aggregation-Induced Emission Luminogens (AIEgens). *ACS Mater. Lett.* **2020**, *2*, 1033−1040.
(29) Dąbrowski, J. M. Reactive Oxygen Species in Photodynamic Therapy: Mechanisms of Their Generation and Potentiation. *Adv. Inorg. Chem.* **2017**, *70*, 343−394.
(30) Li, L.; Shao, C.; Liu, T.; Chao, Z.; Chen, H.; Xiao, F.; He, H.; Wei, Z.; Zhu, Y.; Wang, H.; Zhang, X.; Wen, Y.; Yang, B.; He, F.; Tian, L. An NIR-II-Emissive Photosensitizer for Hypoxia-Tolerant Photodynamic Theranostics. *Adv. Mater.* **2020**, *32*, 2003471.
(31) Zhang, K.; Yu, Z.; Meng, X.; Zhao, W.; Shi, Z.; Yang, Z.; Dong, H.; Zhang, X. A Bacteriochlorin-Based Metal-Organic Framework Nanosheet Superoxide Radical Generator for Photoacoustic Imaging-Guided Highly Efficient Photodynamic Therapy. *Adv. Sci.* **2019**, *6*, 1900530.
(32) Ross, S. M.; Strange, J. H. Pressure and Temperature Dependence of Molecular Motion in Organic Plastic Crystals. *J. Chem. Phys.* **1978**, *68*, 3078−3088.
(33) Bu, F.; Wang, E.; Peng, Q.; Hu, R.; Qin, A.; Zhao, Z.; Tang, B. Z. Structural and Theoretical Insights into the AIE Attributes of Phosphindole Oxide: The Balance between Rigidity and Flexibility. *Chem. - Eur. J.* **2015**, *21*, 4440−4449.
(34) Chen, M.; Zhang, X.; Liu, J.; Liu, F.; Zhang, R.; Wei, P.; Feng, H.; Tu, M.; Qin, A.; Lam, J. W. Y.; Ding, D.; Tang, B. Z. Evoking Photothermy by Capturing Intramolecular Bond Stretching Vibration-Induced Dark-State Energy. *ACS Nano* **2020**, *14*, 4265−4275.
(35) Zor, E.; Oztekin, Y.; Mikoliunaite, L.; Voronovic, J.; Ramanaviciene, A.; Anusevicius, Z.; Bingol, H.; Ramanavicius, A. 1,10-Phenanthroline-5,6-Dione and 9,10-Phenanthrenequinone as Redox Mediators for Amperometric Glucose Biosensors. *J. Solid State Electrochem.* **2014**, *18*, 1529−1536.
(36) Wolf, M. W.; Legg, K. D.; Brown, R. E.; Singer, L. A.; Parks, J. H. Photophysical Studies on the Benzophenones. Prompt and Delayed Fluorescences and Self-Quenching. *J. Am. Chem. Soc.* **1975**, *97*, 4490−4497.
(37) He, Y. Y.; An, J. Y.; Jiang, L. J. Photochemistry of Hypocrellin Derivatives under Anaerobic Conditions. *Chin. Sci. Bull.* **2000**, *45*, 597−603.
(38) Garcia-Diaz, M.; Huang, Y. Y.; Hamblin, M. R. Use of Fluorescent Probes for ROS to Tease Apart Type I and Type II Photochemical Pathways in Photodynamic Therapy. *Methods* **2016**, *109*, 158−166.
(39) Li, M.; Shao, Y.; Kim, J. H.; Pu, Z.; Zhao, X.; Huang, H.; Xiong, T.; Kang, Y.; Li, G.; Shao, K.; Fan, J.; Foley, J. W.; Kim, J. S.; Peng, X. Unimolecular Photodynamic O_2-Economizer to Overcome Hypoxia Resistance in Phototherapeutics. *J. Am. Chem. Soc.* **2020**, *142*, 5380−5388.
(40) Asahi, M.; Kawai, M.; Toyama, T.; Kumagai, Y.; Chuesaard, T.; Tang, N.; Kameda, T.; Hayakawa, K.; Toriba, A. Identification and Quantification of *in Vivo* Metabolites of 9,10-Phenanthrenequinone in Human Urine Associated with Producing Reactive Oxygen Species. *Chem. Res. Toxicol.* **2014**, *27*, 76−85.
(41) Taguchi, K.; Shimada, M.; Fujii, S.; Sumi, D.; Pan, X.; Yamano, S.; Nishiyama, T.; Hiratsuka, A.; Yamamoto, M.; Cho, A. K.; Froines, J. R.; Kumagai, Y. Redox Cycling of 9,10-Phenanthraquinone to Cause Oxidative Stress Is Terminated through Its Monoglucuronide Conjugation in Human Pulmonary Epithelial A549 Cells. *Free Radical Biol. Med.* **2008**, *44*, 1645−1655.
(42) Crawford, P.; Gross, J.; Lawson, K.; Cheng, C.; Dong, Q.; Liu, D.; Luo, Y.; Szczepankiewicz, B.; Heathcock, C. Electrochemical Properties of Some Biologically Active Quinone Derivatives: Furanquinones, Pyridoquinones, and Diplamine, a Cytotoxic Pyridoacridine Alkaloid. *J. Electrochem. Soc.* **1997**, *144*, 3710−3715.

https://doi.org/10.1021/acsnano.1c07730
ACS Nano XXXX, XXX, XXX−XXX

(43) Elgrishi, N.; Rountree, K. J.; McCarthy, B. D.; Rountree, E. S.; Eisenhart, T. T.; Dempsey, J. L. A Practical Beginner's Guide to Cyclic Voltammetry. *J. Chem. Educ.* **2018**, *95*, 197−206.
(44) Tonholo, J.; Freitas, L. R.; de Abreu, F. C.; Azevedo, D. C.; Zani, C. L.; de Oliveira, A. B.; Goulart, M. O. F. Electrochemical Properties of Biologically Active Heterocyclic Naphthoquinones. *J. Braz. Chem. Soc.* **1998**, *9*, 163−169.
(45) Inbaraj, J. J.; Krishna, M. C.; Gandhidasan, R.; Murugesan, R. Cytotoxicity, Redox Cycling and Photodynamic Action of Two Naturally Occurring Quinones. *Biochim. Biophys. Acta, Gen. Subj.* **1999**, *1472*, 462−470.
(46) Johnson, J.; Gandhidasan, I.; Murugesan, R. Cytotoxicity and Superoxide Anion Generation by Some Naturally Occurring Quinones. *Free Radical Biol. Med.* **1999**, *26*, 1072−1078.
(47) Fang, J.; Nakamura, H.; Maeda, H. The EPR Effect: Unique Features of Tumor Blood Vessels for Drug Delivery, Factors Involved, and Limitations and Augmentation of the Effect. *Adv. Drug Delivery Rev.* **2011**, *63*, 136−151.
(48) Kobayashi, H.; Watanabe, R.; Choyke, P. L. Improving Conventional Enhanced Permeability and Retention (EPR) Effects; What Is the Appropriate Target? *Theranostics* **2014**, *4*, 81−89.
(49) Roper, D. K.; Ahn, W.; Hoepfner, M. Microscale Heat Transfer Transduced by Surface Plasmon Resonant Gold Nanoparticles. *J. Phys. Chem. C* **2007**, *111*, 3636−3641.
(50) Tian, Q.; Jiang, F.; Zou, R.; Liu, Q.; Chen, Z.; Zhu, M.; Yang, S.; Wang, J.; Wang, J.; Hu, J. Hydrophilic Cu_9S_5 Nanocrystals: A Photothermal Agent with a 25.7% Heat Conversion Efficiency for Photothermal Ablation of Cancer Cells *in Vivo*. *ACS Nano* **2011**, *5*, 9761−9771.
(51) Setsukinai, K.; Urano, Y.; Kakinuma, K.; Majima, H. J.; Nagano, T. Development of Novel Fluorescence Probes That Can Reliably Detect Reactive Oxygen Species and Distinguish Specific Species. *J. Biol. Chem.* **2003**, *278*, 3170−3175.
(52) Owusu, E. G. A.; MacRobert, A. J.; Naasani, I.; Parkin, I. P.; Allan, E.; Yaghini, E. Photoactivable Polymers Embedded with Cadmium-Free Quantum Dots and Crystal Violet: Efficient Bactericidal Activity against Clinical Strains of Antibiotic-Resistant Bacteria. *ACS Appl. Mater. Interfaces* **2019**, *11*, 12367−12378.
(53) Zhao, X. N.; Dai, Y. P.; Ma, F. L.; Misal, S.; Hasrat, K.; Zhu, H. Y.; Qi, Z. J. Molecular Engineering to Accelerate Cancer Cell Discrimination and Boost AIE-Active Type I Photosensitizer for Photodynamic Therapy under Hypoxia. *Chem. Eng. J.* **2021**, *410*, 128133.
(54) Yang, L.; Wang, X.; Zhang, G.; Chen, X.; Zhang, G.; Jiang, J. Aggregation-Induced Intersystem Crossing: A Novel Strategy for Efficient Molecular Phosphorescence. *Nanoscale* **2016**, *8*, 17422−17426.
(55) Zhang, J.; Mukamel, S.; Jiang, J. Aggregation-Induced Intersystem Crossing: Rational Design for Phosphorescence Manipulation. *J. Phys. Chem. B* **2020**, *124*, 2238−2244.
(56) Xu, S.; Yuan, Y.; Cai, X.; Zhang, C.-J.; Hu, F.; Liang, J.; Zhang, G.; Zhang, D.; Liu, B. Tuning the Singlet-Triplet Energy Gap: A Unique Approach to Efficient Photosensitizers with Aggregation-Induced Emission (AIE) Characteristics. *Chem. Sci.* **2015**, *6*, 5824−5830.
(57) Idris, N. M.; Gnanasammandhan, M. K.; Zhang, J.; Ho, P. C.; Mahendran, R.; Zhang, Y. *In Vivo* Photodynamic Therapy Using Upconversion Nanoparticles as Remote-Controlled Nanotransducers. *Nat. Med.* **2012**, *18*, 1580−1585.
(58) Silva, E. F.; Serpa, C.; Dabrowski, J. M.; Monteiro, C. J.; Formosinho, S. J.; Stochel, G.; Urbanska, K.; Simoes, S.; Pereira, M. M.; Arnaut, L. G. Mechanisms of Singlet-Oxygen and Superoxide-Ion Generation by Porphyrins and Bacteriochlorins and Their Implications in Photodynamic Therapy. *Chem.—Eur. J.* **2010**, *16*, 9273−9286.
(59) Zhao, H.; Joseph, J.; Zhang, H.; Karoui, H.; Kalyanaraman, B. Synthesis and Biochemical Applications of a Solid Cyclic Nitrone Spin Trap: A Relatively Superior Trap for Detecting Superoxide Anions and Glutathiyl Radicals. *Free Radical Biol. Med.* **2001**, *31*, 599−606.
(60) Cai, X.-Y.; Gao, B.; Li, X.-L.; Cao, Y.; Su, S.-J. Singlet-Triplet Splitting Energy Management *via* Acceptor Substitution: Complanation Molecular Design for Deep-Blue Thermally Activated Delayed Fluorescence Emitters and Organic Light-Emitting Diodes Application. *Adv. Funct. Mater.* **2016**, *26*, 8042−8052.
(61) El-Sayed, M. A. Spin-Orbit Coupling and the Radiationless Processes in Nitrogen Heterocyclics. *J. Chem. Phys.* **1963**, *38*, 2834−2838.
(62) Lee, J.; Aizawa, N.; Numata, M.; Adachi, C.; Yasuda, T. Versatile Molecular Functionalization for Inhibiting Concentration Quenching of Thermally Activated Delayed Fluorescence. *Adv. Mater.* **2017**, *29*, 1604856.
(63) Murray, J. S.; Politzer, P. The Electrostatic Potential: An Overview. *Wiley Interdiscip. Rev.: Comput. Mol. Sci.* **2011**, *1*, 153−163.
(64) Scrocco, E.; Tomasi, J. Electronic Molecular Structure, Reactivity and Intermolecular Forces: An Euristic Interpretation by Means of Electrostatic Molecular Potentials. *Adv. Quantum Chem.* **1978**, *11*, 115−193.
(65) Yoo, D. J.; Choi, J. W. Elucidating the Extraordinary Rate and Cycling Performance of Phenanthrenequinone in Aluminum-Complex-Ion Batteries. *J. Phys. Chem. Lett.* **2020**, *11*, 2384−2392.
(66) Lefebvre, C.; Rubez, G.; Khartabil, H.; Boisson, J. C.; Contreras-Garcia, J.; Henon, E. Accurately Extracting the Signature of Intermolecular Interactions Present in the NCI Plot of the Reduced Density Gradient *versus* Electron Density. *Phys. Chem. Chem. Phys.* **2017**, *19*, 17928−17936.
(67) Lu, T.; Chen, F. Multiwfn: A Multifunctional Wavefunction Analyzer. *J. Comput. Chem.* **2012**, *33*, 580−592.
(68) Benov, L.; Sztejnberg, L.; Fridovich, I. Critical Evaluation of the Use of Hydroethidine as a Measure of Superoxide Anion Radical. *Free Radical Biol. Med.* **1998**, *25*, 826−831.
(69) Zielonka, J.; Vasquez-Vivar, J.; Kalyanaraman, B. Detection of 2-Hydroxyethidium in Cellular Systems: A Unique Marker Product of Superoxide and Hydroethidine. *Nat. Protoc.* **2008**, *3*, 8−21.
(70) Zhen, S.; Wang, S.; Li, S.; Luo, W.; Gao, M.; Ng, L. G.; Goh, C. C.; Qin, A.; Zhao, Z.; Liu, B.; Tang, B. Z. Efficient Red/Near-Infrared Fluorophores Based on Benzo[1,2-b:4,5-b′]dithiophene 1,1,5,5-Tetraoxide for Targeted Photodynamic Therapy and *in Vivo* Two-Photon Fluorescence Bioimaging. *Adv. Funct. Mater.* **2018**, *28*, 1706945.

https://doi.org/10.1021/acsnano.1c07730
ACS Nano XXXX, XXX, XXX−XXX